



# Synthesis of ZnAlTi-LDO supported C<sub>60</sub>@AgCl nanoparticles and their photocatalytic activity for photo-degradation of Bisphenol A

Liting Ju<sup>a,b,c,d</sup>, Pingxiao Wu<sup>a,b,c,d,e,\*</sup>, Qiliang Yang<sup>a,b,c,d</sup>, Zubair Ahmed<sup>a,b,c,d</sup>, Nengwu Zhu<sup>a,b</sup>

<sup>a</sup> School of Environment and Energy, South China University of Technology, Guangzhou Higher Education Mega Centre, Guangzhou 510006, PR China

<sup>b</sup> The Key Lab of Pollution Control and Ecosystem Restoration in Industry Clusters, Ministry of Education, Guangzhou 510006, PR China

<sup>c</sup> Guangdong Provincial Engineering and Technology Research Center for Environmental Risk Prevention and Emergency Disposal, South China University of Technology, Guangzhou Higher Education Mega Centre, Guangzhou 510006, PR China

<sup>d</sup> Guangdong Environmental Protection Key Laboratory of Solid Waste Treatment and Recycling, Guangzhou 510006, PR China

<sup>e</sup> Guangdong Engineering and Technology Research Center for Environmental Nanomaterials, Guangzhou 510006, PR China

## ARTICLE INFO

### Keywords:

Photocatalytic  
Core-shell structure  
Bisphenol A  
C<sub>60</sub>@AgCl  
Ag@AgCl-LDO

## ABSTRACT

ZnAlTi layered double oxide (ZnAlTi-LDO) supported C<sub>60</sub>@AgCl nanoparticles were synthesized by the coprecipitation-light-induced method and their photocatalytic activity for photo-degradation of Bisphenol A (BPA) was analyzed quantitatively by high performance liquid chromatography (HPLC). The morphology, structure and composition of the nanocomposites were analyzed by Scanning Electron Microscopy, Transmission electron microscopy, X-ray diffraction patterns, Fourier Transform Infrared spectra and Specific Surface Area. According to the analysis, ZnAlTi-LDO supported C<sub>60</sub>@AgCl nanoparticles (C<sub>60</sub>@AgCl-LDO) was characteristic of mesoporous materials. Pore size distribution plots of all the catalysts were well-distributed, ranging between 10 and 20 nm. Because the heterostructure of Ag@AgCl enhanced near-field for light scattering, reflection and absorption. The Ag@AgCl-LDO nanoparticles and C<sub>60</sub>@AgCl-LDO nanoparticles showed a very intense absorption band in the near-UV region. The C<sub>60</sub> was used as support materials to enhance the stability of Ag-based photocatalysts. The C<sub>60</sub>@AgCl can reduce the recombination of photo-induced electron-hole pairs and therefore increase the efficiency of the photocatalysis. The photo-degradation experiment was conducted by using a series of the nanoparticles to degrade BPA under simulated visible light irradiation. Test results show that, photo-generated holes, superoxide radical species,  $\cdot\text{OH}_{\text{bulk}}$  and singlet oxygen are responsible for the photo-degradation, among which the superoxide radical species plays an indispensable role in the photocatalytic reaction system. The degradation rate of the C<sub>60</sub>@AgCl-LDO in photocatalytic degradation of BPA under simulated visible light irradiation is for 90%. The C<sub>60</sub>@AgCl-LDO nanoparticles with remarkable photocatalytic activity can be used for large-scale environmental remediation.

## 1. Introduction

Bisphenol A (BPA), 4,4'-dihydroxy-2,2-diphenylpropane (CAS no. 80-05-7), is an important organic chemical material and is commonly used as a major monomeric material in the synthesis of polycarbonate plastics and epoxy resins for chemical applications [1–4]. Due to its hardness and strength in a wide temperature range, global production of BPA was exceed 5 million metric tons by 2015 [5,6]. Unfortunately, BPA could cause seriously adverse effects to human beings and wildlife [7,8]. Thus, a great concern has been raised to remove BPA from water and lots of techniques were proposed, such as physical absorption [9], chemical remediation [10,11], and microbial degradation [12]. Among these methods, photocatalytic degradation attracts widespread

attention due to its effective activity and low toxicity. ZnAlTi layered double oxide (ZnAlTi-LDO) has been recently reported in photocatalytic applications, which can meet the cost-effective, green environmental and sustainable approaches in consideration of the even severer global energy crisis [13]. However, the photocatalysis for the degradation of BPA under simulated visible light irradiation does not achieve ideally removing effect by using the materials of ZnAlTi-LDO.

Therefore, it is very necessary to find a desirable photocatalysts with remarkable visible light absorption. Based on the latest study [14–18], silver/silver halide-based compounds (Ag/AgX, X = Cl, Br, I) is considered as potential high-efficiency photocatalysts and photosensitive material. Ag/AgCl heterostructure exhibits strong visible light absorption, owing to the surface plasmon resonance (SPR) [19].

\* Corresponding author at: School of Environment and Energy, South China University of Technology, Guangzhou Higher Education Mega Centre, Guangzhou 510006, PR China.  
E-mail address: [pppxwu@scut.edu.cn](mailto:pppxwu@scut.edu.cn) (P. Wu).

<http://dx.doi.org/10.1016/j.apcatb.2017.10.056>

Received 8 June 2017; Received in revised form 8 October 2017; Accepted 24 October 2017

Available online 04 November 2017

0926-3373/ © 2017 Elsevier B.V. All rights reserved.

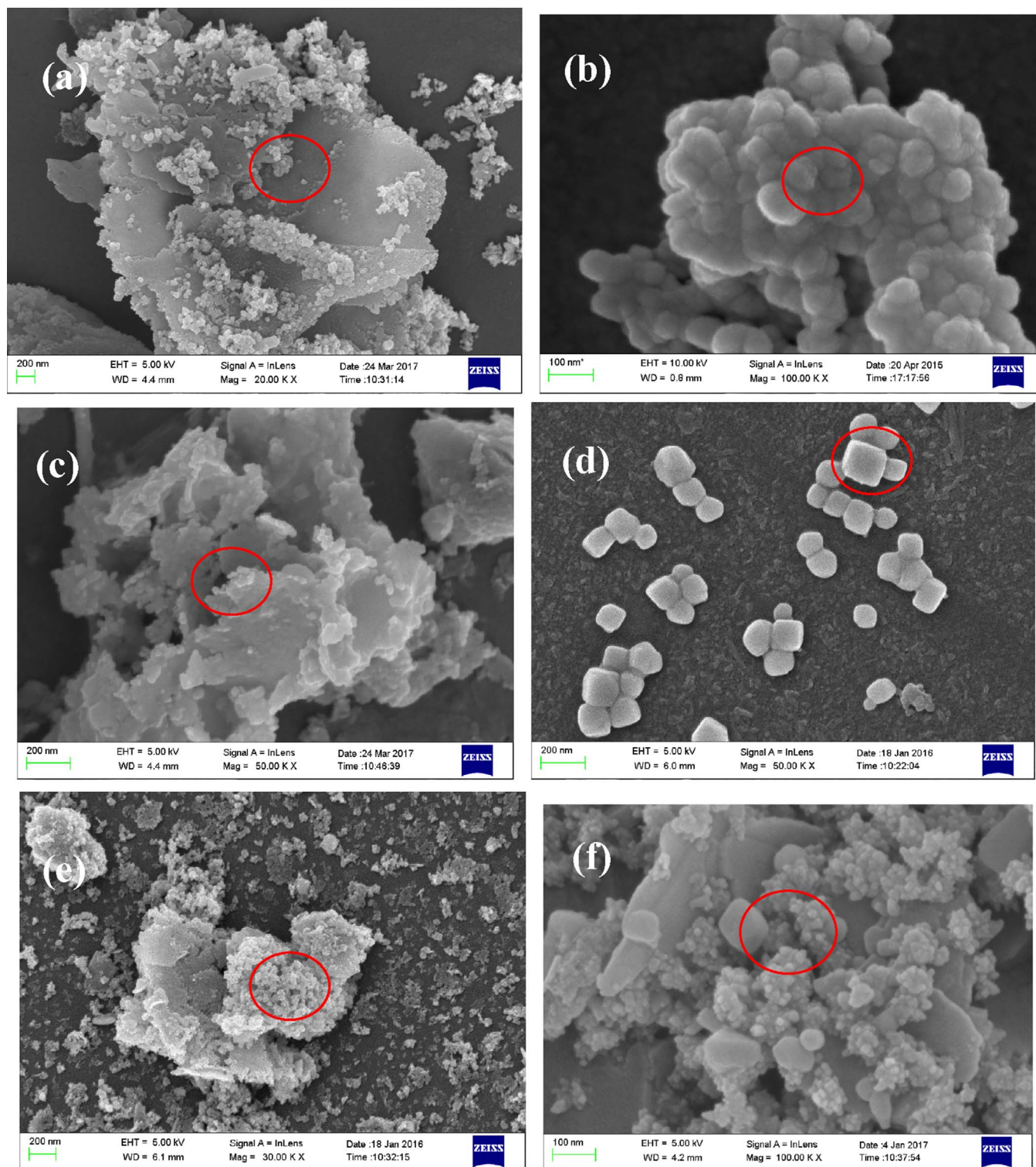


**Fig. 1.** SEM images of: (a) LDO: ZnAlTi-LDO nanoparticles. (b) C<sub>60</sub> nanoparticles. (c) LDO/C<sub>60</sub>-5% nanoparticles. (d) C<sub>60</sub>@AgCl nanoparticles. (e) Ag@AgCl-LDO nanoparticles. (f) C<sub>60</sub>@AgCl-LDO nanoparticles.

Unfortunately, the instability of these photocatalysts greatly limited their practical applications. As is well-known, the AgCl can be resolved to Ag<sup>0</sup>, and then oxidized to Ag<sub>2</sub>O under the UV or visible irradiation easily. This phenomenon will destroy the structure of Ag/AgCl heterostructure and reduces the light energy absorption of Ag/AgCl heterostructure. To enhance the stability of Ag-based photocatalysts, some support materials have been induced by some researchers. They conclude that support materials working as an electron trap can change the

charge transmission to restrain the charge recombination, reducing the photo-corrosion of Ag/AgCl heterostructure [20–25]. Fullerenes (C<sub>60</sub>) is one of the best support materials, with the delocalized conjugated structures. C<sub>60</sub> can be easily formed C<sub>60</sub>@AgCl core-shell structure with the unsaturated bond. There is a corresponding increase in the photocatalytic activity and stability of Ag/AgCl heterostructure.

In this work, C<sub>60</sub>@AgCl modified ZnAlTi-LDO (C<sub>60</sub>@AgCl-LDO) was prepared by the coprecipitation-light-induced method. Photo-



**Table 1**The ICP of LDO, LDO/C<sub>60</sub>-5%, Ag@AgCl-LDO and C<sub>60</sub>@AgCl-LDO.

Elements	LDO mass ration (wt.%)	LDO/C <sub>60</sub> -5% mass ration (wt.%)	C <sub>60</sub> @AgCl-LDO mass ration (wt. %)	Ag@AgCl-LDO mass ration (wt. %)
Zn	69.74	56.97	41.94	42.44
Al	3.92	1.91	2.26	2.12
Ti	10.27	3.29	6.91	5.58
Ag	0.00	0.00	2.97	14.95

degradation experiments were conducted using ZnAlTi-LDO nanoparticles, Ag@AgCl-LDO nanoparticles and C<sub>60</sub>@AgCl-LDO nanoparticles for degradation of BPA under visible light irradiation. The photocatalytic activity of C<sub>60</sub>@AgCl-LDO was enhanced compared with ZnAlTi-LDO. It is postulated that the C<sub>60</sub>@AgCl enhanced photoactivity of ZnAlTi-LDO catalyst results from Ag enhanced near-field and could boost the excitation of electron-hole pairs in ZnAlTi-LDO. And the C<sub>60</sub> enhanced the photoactivity of ZnAlTi-LDO catalyst by its high migration efficiency of photo-induced electron. Photogenerated holes, superoxide radical species,  $\cdot\text{OH}_{\text{bulk}}$  and singlet oxygen were considered to be responsible for the photodegradation by the C<sub>60</sub>@AgCl-LDO. It suggests that C<sub>60</sub>@AgCl-LDO nanoparticles are excellent catalysts for photocatalytic reactions or surface chemical processes.

## 2. Materials and methods

### 2.1. Materials

Bisphenol A (BPA, (CH<sub>3</sub>)<sub>2</sub>C(C<sub>6</sub>H<sub>4</sub>OH)<sub>2</sub>, CAS no. 80-05-7) was bought from the Guangzhou Chemical Reagent Factory (Guangzhou, PRC). The deionized water was used in the preparation processes. Fullerene (C<sub>60</sub>) was purchased from Nanjing in XFNAN. Analytically pure NaCl, AgNO<sub>3</sub>,

ZnCl<sub>2</sub>, AlCl<sub>3</sub>·6H<sub>2</sub>O, TiCl<sub>4</sub>, HCl, Na<sub>2</sub>SO<sub>4</sub>, Sodium oxalate (Na<sub>2</sub>C<sub>2</sub>O<sub>4</sub>), C<sub>8</sub>H<sub>6</sub>O<sub>4</sub>(TAOH), NaOH, NaF, NaN<sub>3</sub>, Nafion emulsion, Ethylene glycol (EG, (CH<sub>2</sub>OH)<sub>2</sub>), Polyvinylpyrrolidone (PVP, CAS:9003-39-8, (C<sub>6</sub>H<sub>9</sub>NO)<sub>n</sub>), Benzoquinone (BQ, C<sub>6</sub>H<sub>4</sub>O<sub>2</sub>), Isopropanol (ISO, (CH<sub>3</sub>)<sub>2</sub>CHOH), Methanol (MeOH, CH<sub>3</sub>OH) and urea were used without further purification and purchased from the Guangzhou Chemical Reagent Factory.

### 2.2. Sample preparation by coprecipitation-light-induced method

The ZnAlTi-LDO was synthesized by utilizing urea hydrolysis [13]. The synthetic procedure was as follows:  $6 \times 10^{-2}$  mol of ZnCl<sub>2</sub>,  $5.3 \times 10^{-3}$  mol of AlCl<sub>3</sub>·6H<sub>2</sub>O, 1.20 mL of TiCl<sub>4</sub> solution (the solution was prepared by TiCl<sub>4</sub> and HCl with a volume ratio of 1:1, TiCl<sub>4</sub> was  $1.06 \times 10^{-2}$  mol), 0.58 mol of urea were dissolved in 250 mL deionized water under vigorous stirring [26]. The resulting dispersion was stirred for 48 h at 110 °C refluxing condition. The materials washed thoroughly with deionized water several times and dried in a vacuum oven at 60 °C for 12 h. The samples were denoted as ZnAlTi-LDH (LDH). The dried products were vacuum calcined for 5 h at 500 °C, the samples were denoted as ZnAlTi-LDO (LDO).

The C<sub>60</sub>@AgCl-LDO was successfully synthesized by the coprecipitation-light-induced method. In the process, the EG was added as solvent, the PVP added in the solution as structure directing agent and stabilizer. The ZnAlTi-LDO, PVP, C<sub>60</sub> and AgNO<sub>3</sub> were added into a 500 mL beaker, while the mass ratio was 67: 100: 8: 28. These materials were dissolved into EG solution. The molar ratio of NaCl and AgNO<sub>3</sub> was 1:1, and NaCl was dissolved into EG solution in a 100 mL beaker. The synthetic procedure was as follows: 1.2 g ZnAlTi-LDO, 0.51 g AgNO<sub>3</sub>, 0.1485 g C<sub>60</sub>, 1.8 g PVP and 120 mL EG were added into a 500 mL beaker for mixing under vigorous stirring. 0.18 g NaCl and 30 mL EG were added into a 100 mL beaker for mixing under vigorous stirring. Then, the NaCl solution was added into the first 500 mL beaker

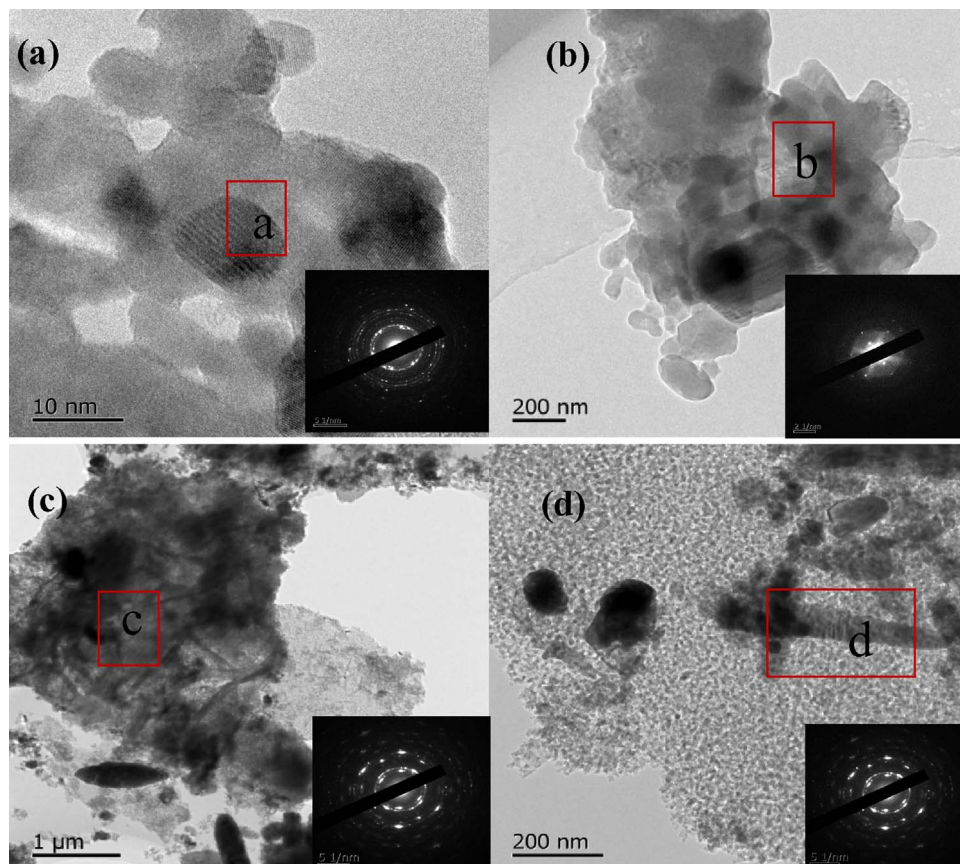


**Fig. 2.** TEM images of: (a) LDO: ZnAlTi-LDO nanoparticles and the electron diffraction of LDO. (b) C<sub>60</sub> nanoparticles and the electron diffraction of C<sub>60</sub>. (c) LDO/C<sub>60</sub>-5% nanoparticles and the electron diffraction of LDO/C<sub>60</sub>-5%. (d) C<sub>60</sub>@AgCl-LDO nanoparticles and the electron diffraction of C<sub>60</sub>@AgCl-LDO.

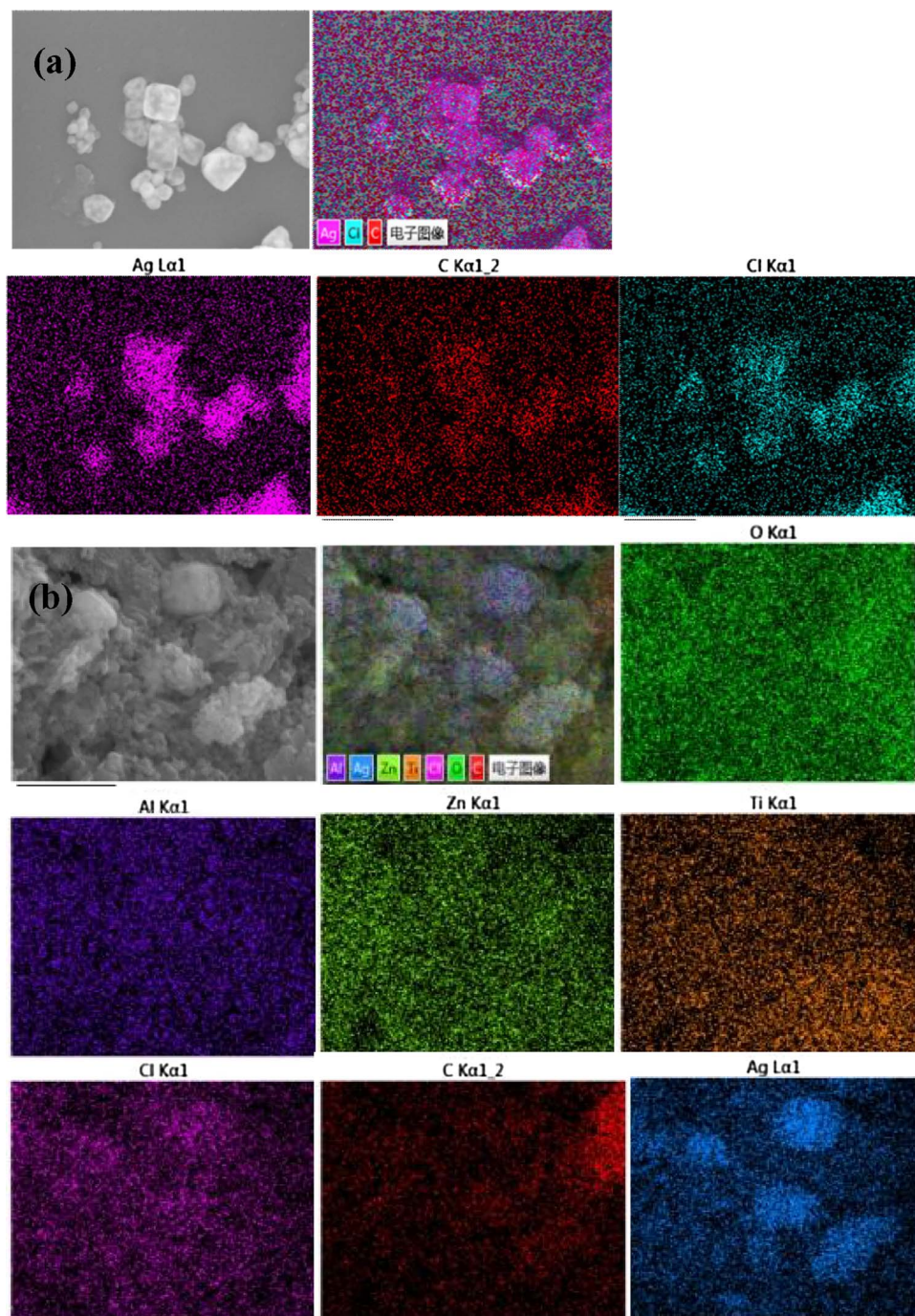


Fig. 3. EDS images of (a)  $C_{60}@AgCl$  nanoparticles and (b)  $C_{60}@AgCl$ -LDO nanoparticles.

by drops. Coprecipitation reaction lasted for 24 h. To obtain the metallic Ag, a 300W xenon lamp was used as the luminous energy to illuminate the suspension for 10 min after the coprecipitation reaction. This materials were dried in a vacuum oven at 60 °C for 12 h after washing thoroughly with deionized water several times, and the sample was denoted as  $C_{60}@AgCl$ -LDO. The materials were prepared without  $C_{60}$  according to the above steps, and the sample was denoted as  $Ag@AgCl$ -LDO. The LDO/ $C_{60}$ -5% was also synthesized by the coprecipitation-light-induced method. The mass ratio of  $C_{60}$  to ZnAlTi-LDH was 5: 100.

### 2.3. Characterization

The external surface and microstructure of the samples were

observed by a ZEISS Merlin Scanning electron microscopy (SEM, Carl Zeiss, Germany). The chemical composition of this materials was characterized by EDS analysis (Bruker, Quantax EDS detector). High-resolution transmission electron microscopy (TEM) images were obtained by JEM-2100F field emission transmission electron microscope with an accelerating voltage of 200 kV. Inductively Coupled Plasma (ICP) analysis provides fast identification and detection of metals content in chemical samples. The X-ray diffraction (XRD) patterns were measured by an X-ray diffractometer (D/MAX-III A, Rigaku Ltd., Japan) equipped with Cu Kα radiation. The Fourier transform infrared (FT-IR) spectra of the samples were collected by a PerkinElmer 1725X FT-IR spectrometer using KBr pellets, in the range of 4000–400  $cm^{-1}$  with 4  $cm^{-1}$  resolution. The measurement of particle surface areas and pore sizes was carried out by  $N_2$  adsorption-desorption isotherm analysis

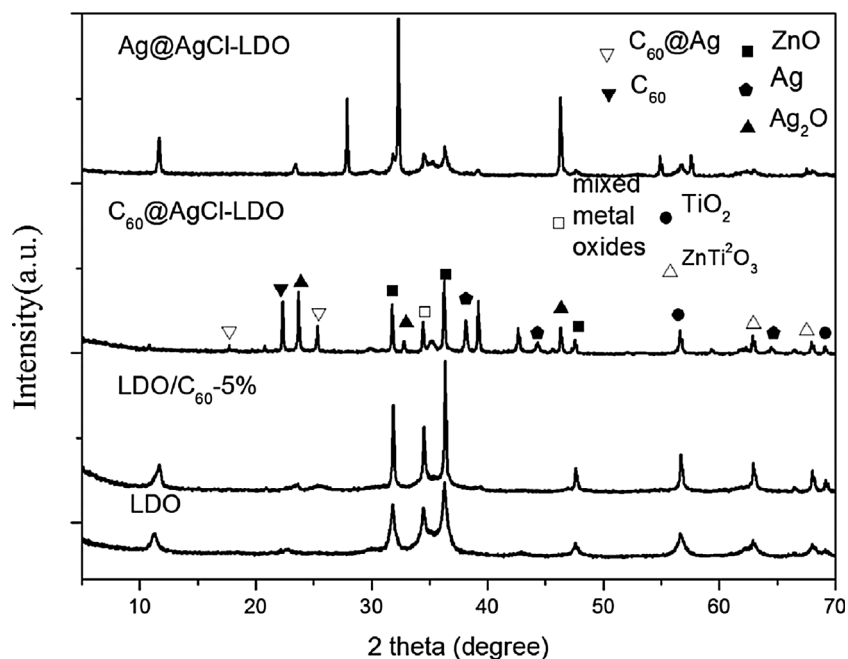


Fig. 4. Powder X-ray diffraction patterns of: ZnAlTi-LDO nanoparticles, LDO/C<sub>60</sub>-5% nanoparticles, Ag@AgCl-LDO nanoparticles and C<sub>60</sub>@AgCl-LDO nanoparticles. The 2θ from 5° to 70°.

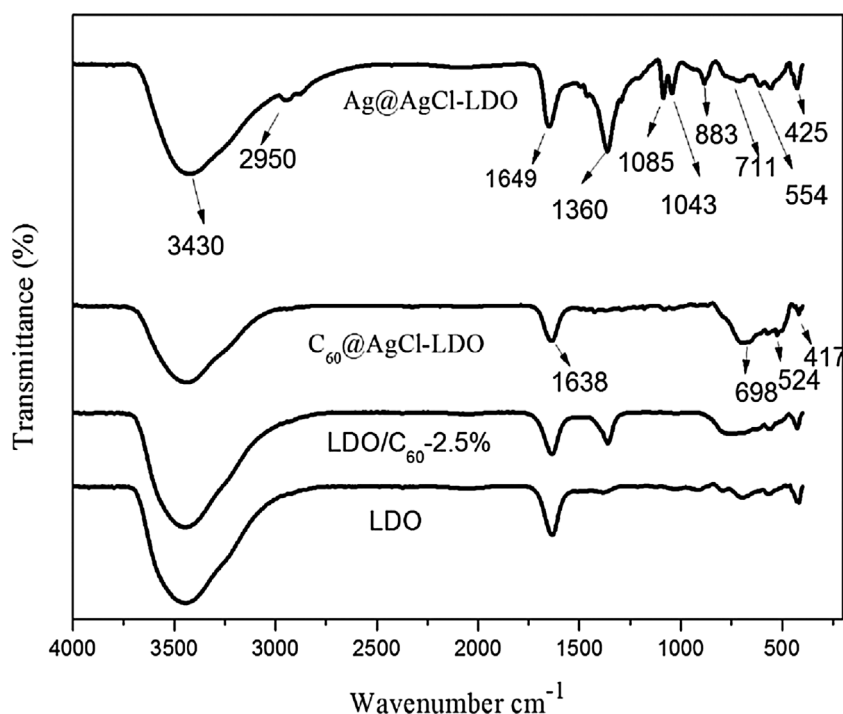


Fig. 5. FTIR spectra of ZnAlTi-LDO nanoparticles, LDO/C<sub>60</sub>-2.5% nanoparticles, C<sub>60</sub>@AgCl-LDO nanoparticles and Ag@AgCl-LDO nanoparticles.

with a Chemisorption Specific Surface Area (SSA) Analyzer (ASAP 2010, Micromeritics, America). Solid state UV–vis diffuse reflectance spectra (UV-vis DRS) was recorded on Shimadzu UV-2501PC spectrometer within 200–800 nm wavelength range at room temperature. Photoluminescence data (PL) was acquired using an F-7000 fluorescence spectrophotometer (Hitachi, Japan). The X-ray photoelectron spectra (XPS) analyses were obtained by an X-ray photoelectron spectrometer (AES430S, ANELVA, Japan). Transient photocurrent response were recorded in 0.1 M Na<sub>2</sub>SO<sub>4</sub> electrolyte solution by using an electrochemical workstation (CHI660E, Shanghai Chenhua Instrument Co., China) with three-electrode system at room temperature. Ag/AgCl and a platinum foil served as reference and counter electrode; respectively. The working electrode was a glassy carbon disk, modified with catalysts

to form the catalysts layer. The working electrode was made as follow: 2 mg catalyst was ultrasonically dispersed in 2 mL ethanol to form suspension and then 10 μL Nafion emulsion was added into the suspension. 10 μL of this suspension was deposited onto the surface of glassy carbon disk and dried at room temperature for electrochemical test. As for transient photocurrent response test, the light source was a 300W xenon lamp and the transient photocurrent of the photocatalysts responded to the light on or off was recorded at 0.0 V to stimulate real photocatalysis reaction condition. The decrease in total organic carbon (TOC) was evaluated by Apollo 9000 TOC analyzer. The Gas Chromatography-Micro Mass (GC–MS) was measured by QP 2010 Ultra GC–MS analyzer (Shimadzu, Japan).



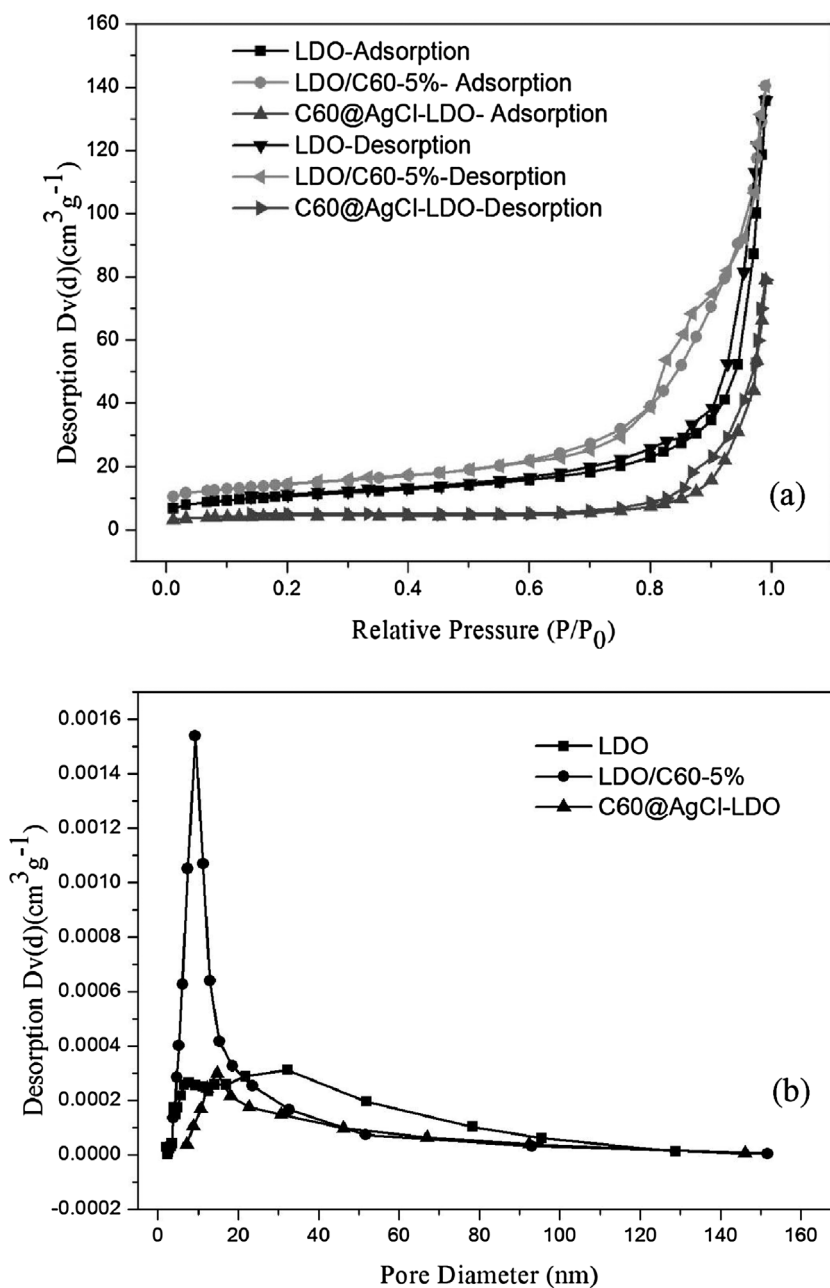


Fig. 6. (a)  $N_2$  adsorption- desorption isotherms and (b) pore size distribution of the obtained samples.

**Table 2**  
Specific surface area analysis and textural parameters of the samples.

Samples	$S_{BET}$ ( $m^2/g$ )	$S_{ext}$ ( $m^2/g$ )	$S_{micro}$ ( $m^2/g$ )	$D_{aver}$ (nm)	$V_{total}$ ( $cm^3/g$ )	$V_{micro}$ ( $\times 10^{-3} cm^3/g$ )
LDO	37.97	29.16	8.8040	14.21	0.13	3.74
LDO/C <sub>60</sub> -5%	50.17	32.44	17.7373	13.29	0.17	8.03
C <sub>60</sub> @AgCl-LDO	15.27	5.72	9.5501	17.86	0.07	4.30

#### 2.4. Photocatalytic experiments

The photocatalytic activity of the samples for the degradation of BPA was measured by exposing them in simulated visible light. Simulated visible light was provided by a 300W xenon lamp. Appropriate amounts of catalyst (0.1 g) were added to 200 mL BPA solution (10 mg/L) in the reaction kettle, and then vigorously stirred in the dark for 60 min to establish the adsorption equilibrium. The

suspension was then irradiated with simulated visible light for 4 h. During the irradiation, at intervals of 0.5 h, the samples (2 mL) filtered through a 0.2  $\mu m$  polyethersulfone. The syringe-filters of the suspension were collected and the samples were analyzed quantitatively with HPLC. The BPA content was analyzed quantitatively by high performance liquid chromatography (HPLC, Hitachi, L-2000), and a C18 column (250 mm  $\times$  4.6 mm, 5  $\mu m$  particle sizes) was used for separation. Millennium 32 software was employed to acquire and process chromatographic data. The mobile phase was a mixture of acetonitrile/water (50:50, volume ratio), and the flow rate was 1.0 mL/min. The column temperature was controlled at 28  $^{\circ}C$ . The injection volume of the column effluent was 20  $\mu L$  and monitored at 276 nm.

### 3. Results and discussions

#### 3.1. Composition and structure

Fig. 1a presents the ZnAlTi-LDH sheets possess high crystallinity.

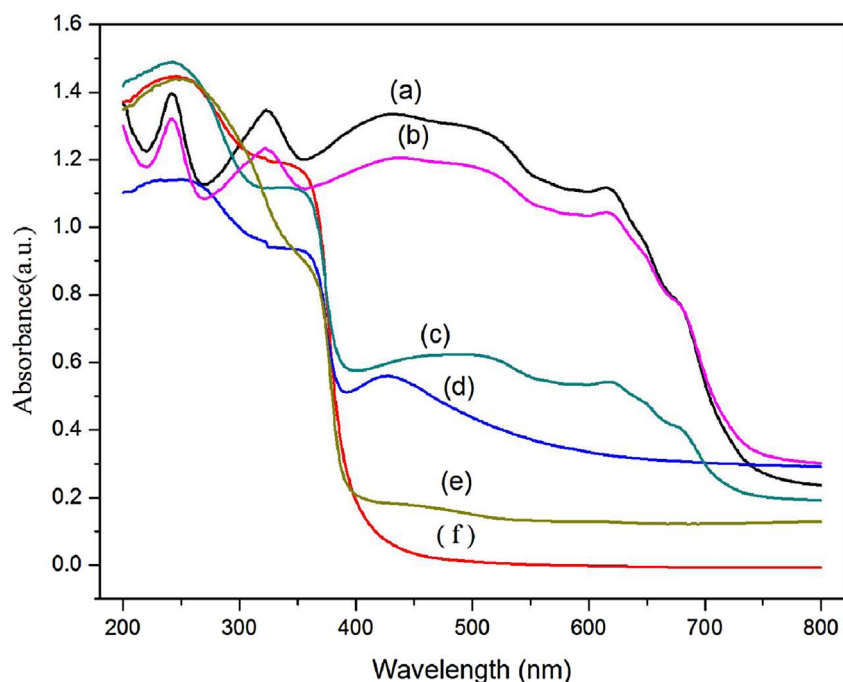


Fig. 7. UV-vis DRS for the prepared materials: (a)  $C_{60}$  nanoparticles, (b)  $C_{60}@AgCl$  nanoparticles, (c)  $C_{60}@AgCl-LDO$  nanoparticles, (d)  $Ag@AgCl-LDO$  nanoparticles, (e)  $LDO/C_{60}-5\%$  nanoparticles, (f)  $LDO$  nanoparticles.

Fig. 1b presents a SEM image of  $C_{60}$  and it shows that the  $C_{60}$  is easy reunion. According to Fig. 1c and Table 1, the  $C_{60}$  nanoparticles is distributed on the  $LDO/C_{60}-5\%$ . Fig. 1d–f presents that the nanoparticles dispersed well and the core-shell structure of  $C_{60}@AgCl$  looks like a dice with six sides, indicating a good combination between the  $C_{60}@AgCl$  and  $ZnAlTi-LDO$  crystals [19,24]. Fig. 2a displays the HRTEM images of  $LDO$ . The electron diffraction of  $LDO$  shows a set of uniform lattice fringes providing further evidence in favour of crystalline nature of nanoparticles. The electron diffraction of  $C_{60}$  shows that the structure of  $C_{60}$  is single crystal structure (Fig. 2b). According to Fig. 2c, the  $LDO/C_{60}-5\%$  nanoparticles is stratified structure. The spatial distribution of the Zn, Al, Ti, Ag, Cl and C elements was further determined using EDS mapping analysis. As Fig. 3 revealed, Zn, Al and Ti are homodisperse throughout the entire material. Ag, Cl and C elements are concentrated on the hexahedron. It can be seen from Figs. 2d and 3 that  $C_{60}$  and Ag formed the  $C_{60}@AgCl$  or  $Ag@AgCl$  core-shell structure like a dice or rod, and it is supported by  $LDO$  [24,27].

The XRD patterns of the samples show small reflections at  $12^\circ$ . From Fig. 4, it can be observed that small proportion of layer structure still remained after calcination. The  $d_{003}$  of  $ZnAlTi-LDO$ ,  $LDO/C_{60}-5\%$  and  $C_{60}@AgCl-LDO$  were respectively 7.82 Å, 7.55 Å and 8.18 Å. Using the  $LDO$  as the supporter as shown in Fig. 4 and Table 1, all the catalysts had the same characteristics of  $LDO$ , and all the catalysts shows the mixed metal oxide phase at  $\sim 35^\circ$ . The mixed metal oxide at  $\sim 35^\circ$  plays an important role in the photocatalytic degradation [13,28]. In addition, the diffraction peaks at about  $44.4^\circ$  and  $64.5^\circ$  can be assigned to both  $Ag^0$  and  $AgCl$ . It is noticeable that the characteristic peak of  $Ag^0$  at  $38.1^\circ$  was found in the materials of  $C_{60}@AgCl-LDO$  and  $Ag@AgCl-LDO$  [29].  $C_{60}$  exhibit characteristic signals in the range of  $10-32^\circ$  which can be indexed as  $22.5^\circ$ , and  $C_{60}@Ag$  shows additional signals which could be indexed to  $18^\circ$  and  $25.5^\circ$  [30]. Furthermore, the diffraction peaks of mixed metal oxides increased with the adding  $C_{60}$  and Ag content in the samples, and the diffraction peaks of  $C_{60}@AgCl-LDO$  are stronger than those of the  $LDO$  sample. That means the Ag exist in the  $C_{60}@AgCl-LDO$  and  $Ag@AgCl-LDO$ , and had a great influence in the materials.

FT-IR analysis provided information regarding the nature of the anions from the interlayers, and the relative spectra ( $4000-400\text{ cm}^{-1}$ ) of all synthesized materials are shown in Fig. 5. The intense broad band around  $3430\text{ cm}^{-1}$  was associated with the stretch of O–H in the

brucite-like layer and water molecules existing in the interlayer space [29]. A weak shoulder around  $2950\text{ cm}^{-1}$  was ascribed to the –OH stretching vibration of interlayer water and hydrogenbonded to interlayer carbonate anions. The weak band record around  $1638\text{ cm}^{-1}$  in all cases is due to the bending mode of water molecules. These bands presents that the  $LDO$  is the supporter, which is not changed by the  $C_{60}$  and Ag. The bending mode of carbonate ions attributed at  $1043\text{ cm}^{-1}$  by observing the weak band. Despite the fact that this band was IR-inactive in the free carbonate, it became activated owing to reduce the symmetry of carbonate anion in the interlayer. Besides, the bands at low frequency region (below  $1000\text{ cm}^{-1}$ ) are corresponding to vibration of metal oxygen and deformation, other modes of carbonate species and vibration of metal-oxygen-metal stretching [31]. While the splitting occurred from the restricted symmetry in the interlayer space.  $Ti^{4+}$  cations of the brucite-like layer made a strong electrostatic attraction between the layer and the interlayer carbonate anions, strengthening the symmetries of the interlayer anions [32,33]. The appearance of absorbance band at  $1085\text{ cm}^{-1}$  in the spectrum of  $C_{60}@AgCl-LDO$  nanocomposite related to Van der Waals forces between Ag and C–C bonds. The unsaturated bond of  $C_{60}$  and Ag changed the balance of chemical bonds, and the band of Ag oxide exited at  $711\text{ cm}^{-1}$ .

The nitrogen adsorption–desorption measurement was carried out in order to give a further insight into the SSA and porosity of the calcined samples. Fig. 6 presents the nitrogen adsorption–desorption isotherms as well as the corresponding pore size distribution curve for  $ZnAlTi-LDO$ ,  $LDO/C_{60}-5\%$  and  $C_{60}@AgCl-LDO$  samples. The SSA, pore volumes and relative information of all the catalysts were listed in Table 2. The samples exhibited typical IV isotherm, which is the typical characteristic of mesoporous materials, according to IUPAC classification [34]. Hysteresis loop of the type was  $H_3$ , which had no limiting adsorption at  $p/p_0$  close to 1 and was commonly giving rise to slit-shaped pores generated by the aggregation of plate-like particles. The measured SSA of  $LDO$ ,  $LDO/C_{60}-5\%$  and  $C_{60}@AgCl-LDO$  samples were  $37.97\text{ m}^2/\text{g}$ ,  $50.17\text{ m}^2/\text{g}$  and  $15.27\text{ m}^2/\text{g}$ , respectively. Because the sample was made by the coprecipitation method, the SSA of  $C_{60}@AgCl-LDO$  become smaller and the pore size distribution of the samples was uniform. The pore size distribution plots of all the catalysts are well-distributed, ranging between 10 and 20 nm.

In order to observe the photocatalytic performance of catalysts, UV-vis diffuse reflectance spectroscopy studies were performed

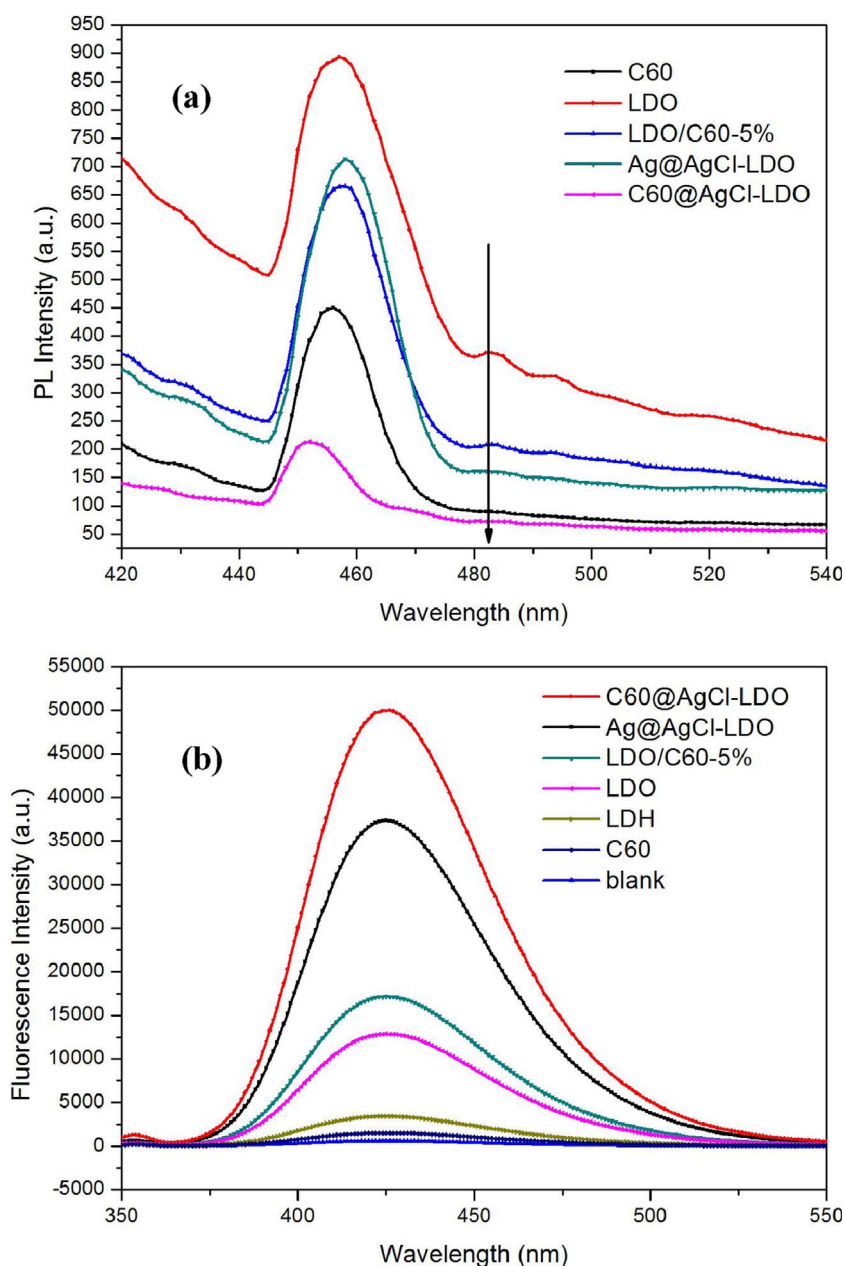


**Fig. 8.** (a) PL emission spectra of the prepared materials (b) room-temperature photoluminescence (PL) spectra of TAOH from reaction solution without addition of BPA in the presence of  $5 \times 10^{-4}$  M of TAOH and  $2 \times 10^{-3}$  M NaOH after 1 h irradiation.

(Fig. 7). The adsorption spectrum of ZnAlTi-LDO in the region 200–400 nm can be attributed to the ligand-to-metal charge transfer involving Zn and Ti atoms in octahedral coordination within the layered network. The UV–vis diffuse reflectance spectra indicated that the incorporation of C<sub>60</sub> and Ag expanded the absorption of ZnAlTi-LDO into visible-light region. Comparison of the materials' corresponding absorption spectra clearly shows that the C<sub>60</sub>@AgCl-LDO composites enhanced absorption in the visible light region (400–800 nm) with the adding C<sub>60</sub> and Ag content. Therefore, that's why the C<sub>60</sub>@AgCl-LDO photo-degradation of BPA is best [19,20,35]. In addition, Ag@AgCl-LDO and C<sub>60</sub>@AgCl-LDO show a very intense absorption band in the near-UV region. This is because of the visible light response with Ag@AgCl and the unique hierarchical structure for the light scattering, reflection and absorption [23,24,35]. We therefore hypothesized that Ag enhanced the absorption of ZnAlTi-LDO into the near-UV region. Due to its photo-absorptive characteristic, the C<sub>60</sub> can absorb electrons from photo-induced irradiation and transfer them to ZnAlTi-LDO, increasing the electron density. The electron migration away from AgCl could significantly inhibit the reaction, and C<sub>60</sub> capture electrons to

guarantee the stability of the composite. The electrons from the photo-excited AgCl could be injected into Ag and immediately transfer to the conduction band (CB) of ZnAlTi-LDO [24,25,55]. The core-shell structure of C<sub>60</sub>@AgCl or Ag@AgCl enhances light absorption of ZnAlTi-LDO. That is a synergetic effect among C<sub>60</sub>, AgCl and Ag in the ZnAlTi-LDO nanocomposites, which is favorable to the visible light photocatalytic activity of C<sub>60</sub>@AgCl-LDO composites.

The transfer of the photo-induced electrons and holes would cause variations in photoluminescence (PL) signal of material. The PL emission spectra of materials presented that C<sub>60</sub>@AgCl-LDO exhibited higher photocatalytic activity than ZnAlTi-LDO, and the PL emission spectra was examined in the 420–540 nm wavelength range ( $\lambda_{\text{ex}} = 350$  nm) [36]. As shown in Fig. 8a, ZnAlTi-LDO shows an emission peak at 458 nm approximately, corresponding to the recombination of photo-induced electron-hole pairs, whereas the observed PL intensity of Ag@AgCl-LDO and LDO/C<sub>60</sub>-5% composite were much weaker than that of ZnAlTi-LDO. As for C<sub>60</sub>@AgCl-LDO sample, the recombination of photoinduced electron-hole pairs was inhibited greatly due to the superior electrical conductivity of C<sub>60</sub> and the strong



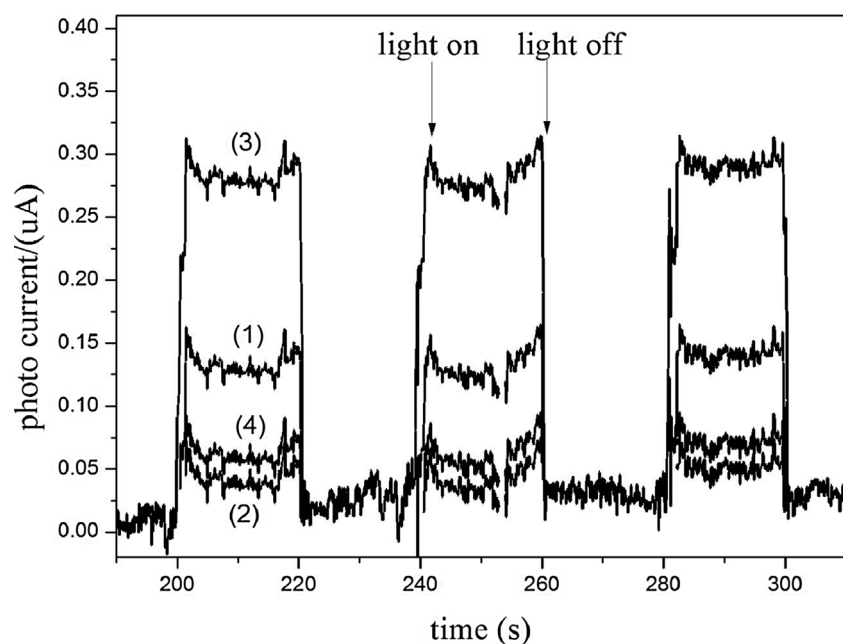


Fig. 9. Transient photocurrent response of (1)  $C_{60}$  nanoparticles; (2) LDO nanoparticles; (3)  $C_{60}@AgCl$ -LDO nanoparticles; (4)  $Ag@AgCl$ -LDO nanoparticles.

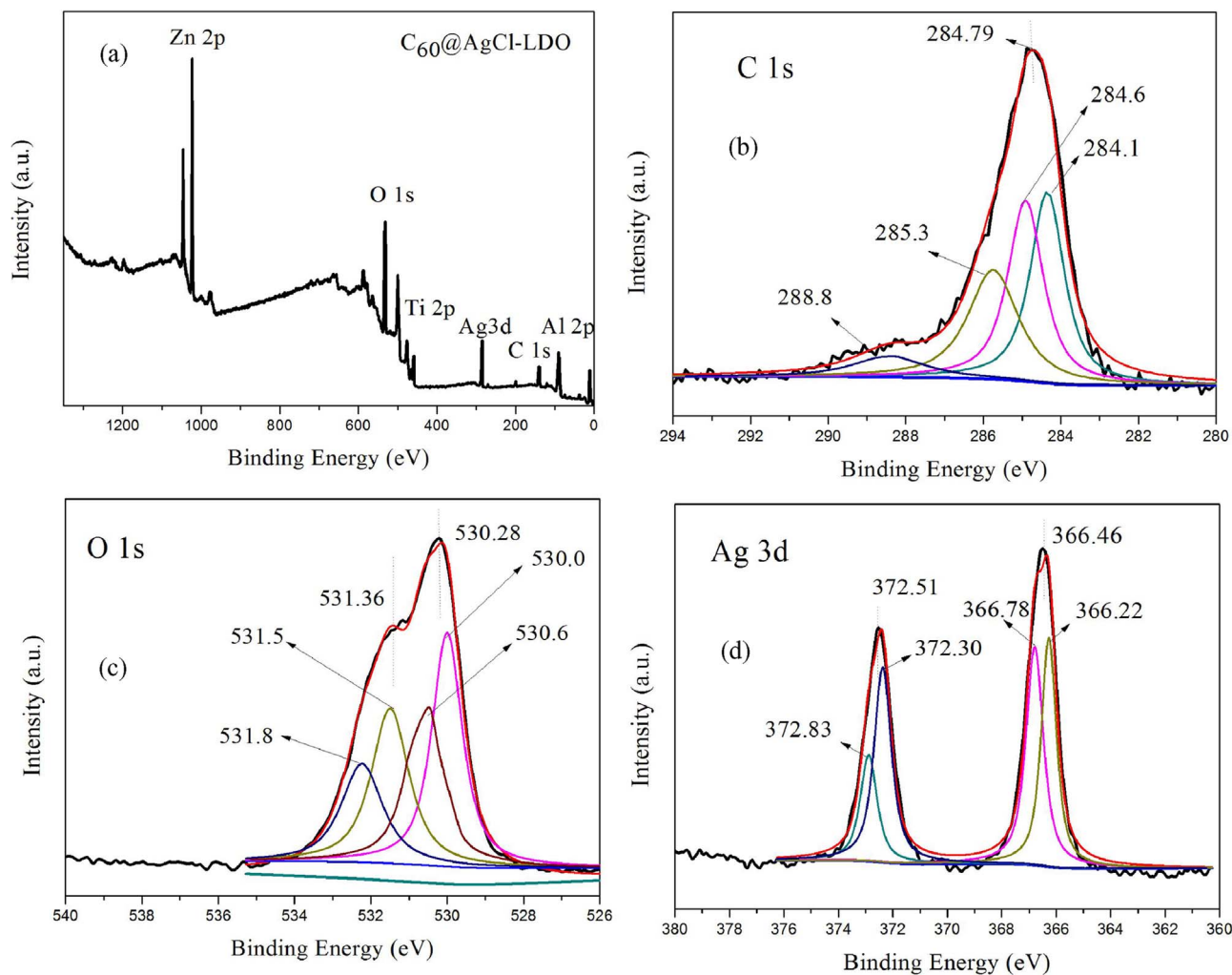


Fig. 10. XPS spectra of  $C_{60}@AgCl$ -LDO nanoparticles: (a) XPS survey spectrum, (b) high resolution  $C_{1s}$  spectrum, (c) high resolution  $O_{1s}$  spectrum (d) high resolution  $Ag_{3d}$  spectrum.

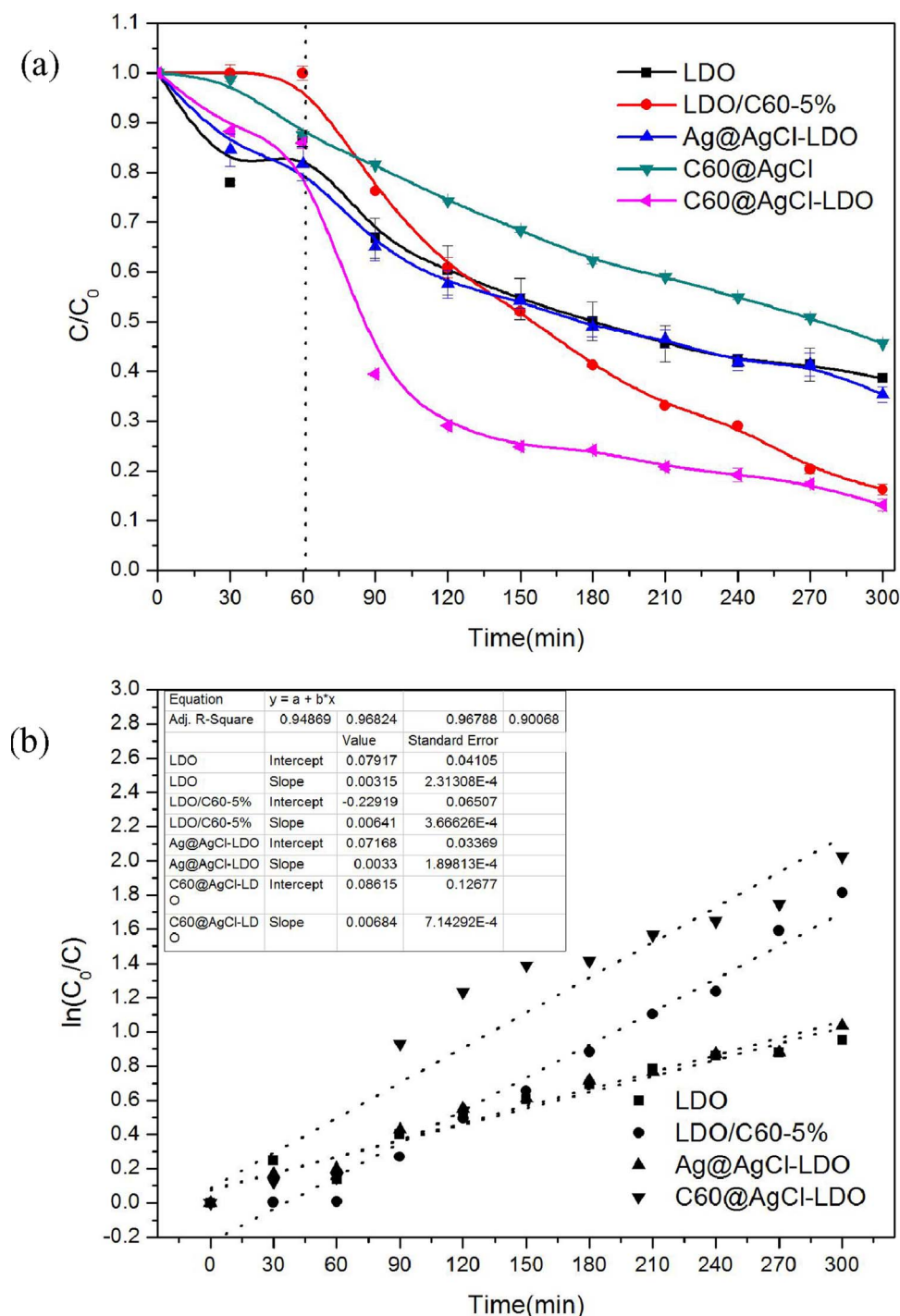


Fig. 11. (a) The effect of  $C_{60}$  and Ag loading with different composition on the reduction of Bisphenol A (b)  $\ln(C_0/C)$  with visible light irradiation time use different materials (experimental conditions: 10 mg/L BPA, reaction dose 0.5 g/L, pH = 7, temperature 28 °C) Each data represents mean  $\pm$  standard error (n = 3).

coupling between ZnAlTi-LDO and  $C_{60}$ @AgCl [24,25,35]. As for  $C_{60}$ -added photocatalysts, the enhanced carrier transfer is contributed mainly by the enhanced spatial charge transportation properties of  $C_{60}$ . As for Ag-added photocatalysts, the decreased electron-hole recombination is contributed mainly by the changed surface states of materials [37]. To explore the mechanism of BPA photo-degradation, the formation of active hydroxyl radicals ( $\cdot OH$ ) upon irradiation was monitored, which is typically considered as the most important oxidative intermediate in photocatalytic reactions. Furthermore, the formation of  $\cdot OH$  radical was also observed by PL spectra in the presence of terephthalic acid (TA) as a probe reagent in the photocatalytic reaction system instead of BPA [35,36]. It is well known that  $\cdot OH$  radical can react readily with TA to generate a strong fluorescent product, 2-

hydroxyterephthalic acid (TAOH) and the intensity of PL for TAOH is proportional to the amount of produced  $\cdot OH$  radicals. As shown in Fig. 8b, on the basis of the intensity of PL for TAOH ( $\lambda_{ex} = 315$  nm), the amount of the produced  $\cdot OH$  radicals on  $C_{60}$ @AgCl-LDO and Ag@AgCl-LDO are larger than that on ZnAlTi-LDO after 1 h simulated light irradiation, suggesting a higher separation efficiency of photo-induced electron-hole pairs and a lower recombination electron-hole for  $C_{60}$ @AgCl-LDO sample [19–23,35]. Fig. 9 shows the I-t curves for the four samples under visible light irradiation. The photocurrent was determined mainly by the separated efficiency of the photo-generated electron-hole pairs within the photocatalyst [36]. The high specific surface area and the  $\pi$ - $\pi$  stacking interactions of  $C_{60}$  were responsible for improving the BPA concentration near the photocatalyst surface. Ag

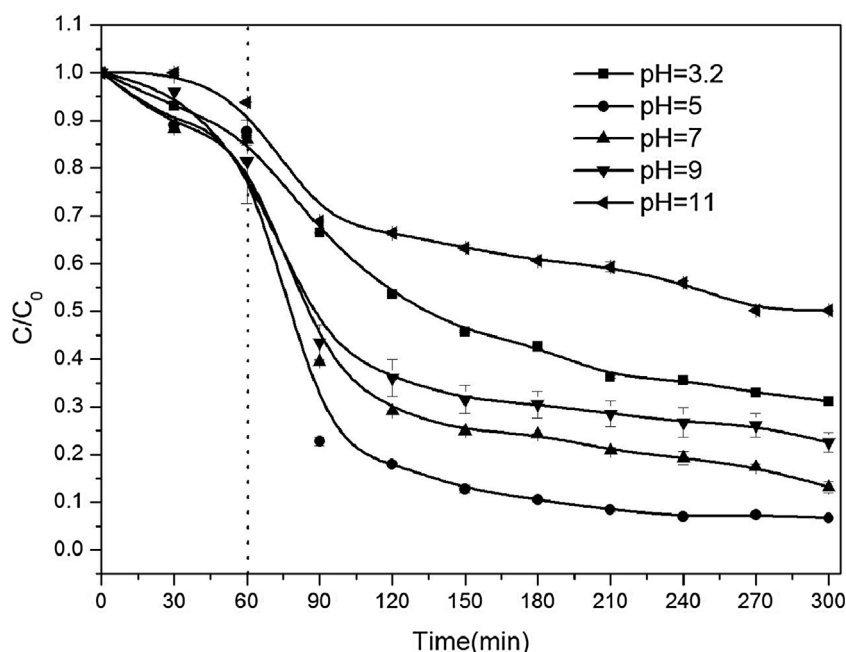


Fig. 12. The effect of different initial pH on the reduction of Bisphenol A (experimental conditions: 10 mg/L BPA, reaction dose 0.5 g/L, temperature 28 °C) Each data represents mean  $\pm$  standard error ( $n = 3$ ).

and  $C_{60}$  can decreased electron-hole recombination and improve the photocurrent to increase the reaction rate [37].

10a. shows the XPS survey spectrum for  $C_{60}@AgCl-LDO$ . As expected, it contained C, O and Ag elements. The regional C1 s spectrum displays an asymmetric and broad peak, suggesting the co-existence of distinguishable models (Fig. 10b). This C1 s peak could be separated into four peaks, which were the binding energies respectively at 284.1 eV, 284.6 eV, 285.3 eV and 288.8 eV. The main peak located at 284.1 eV and 284.6 eV were assigned to adventitious carbon and sp<sup>2</sup> carbon from the  $C_{60}$ . The peak located at 285.3 eV was attributed to defect containing sp<sup>2</sup> carbon. In addition, there was a relatively weak peak located at 288.8 eV, corresponding to carboxyl carbon (O=C–O) and/or Ti–O–C bonds. The O1 s XPS spectrum illustrated in Fig. 10c could be separated into five peaks. The peak at 531.8 eV was ascribable to Ti–OH and/or C=O and O–C=O, and the peaks at 530.0 eV was ascribable to oxygen anions in the lattice (Ti–O–Ti). The peak at 530.6 eV may be assigned to carbonyl oxygen of O=C–O–Ti bonds or residual –COOH [36,38]. The peaks at binding energy of 531.5 eV and 531.8 eV were ascribable to  $Ag_2O$ . Two typical peaks of Ag3d located at 366.46 eV and 372.51 eV can be attributed to the  $Ag3d_{5/2}$  and  $Ag3d_{3/2}$  binding energies, respectively (Fig. 10d). The  $Ag3d_{5/2}$  peak and  $Ag3d_{3/2}$  peak can be further divided into two different peaks. Specifically, the peaks at 366.22 eV and 372.83 eV are attributed to metallic Ag<sup>0</sup>, and those at 366.78 eV and 372.30 eV are attributed to be Ag<sup>+</sup> of AgCl. This result of Ag3d spectrum indicates the co-existence of metallic Ag and AgCl in the composites [24,39,40].

### 3.2. Influencing factors of photocatalytic degradation

#### 3.2.1. Effect of $C_{60}$ or Ag modified ZnAlTi-LDO

According to Fig. 11, the  $C_{60}@AgCl-LDO$  nanoparticles was better than ZnAlTi-LDO nanoparticles for BPA reduction. As we know the adsorption of pollutants on catalyst is an acritical step for their followed degradation reactions since the photocatalyst degradation occurred mainly on the catalyst surface. The reaction of the materials degraded BPA reached the adsorption equilibrium for one hour under dark. Fig. 11a shows that the physical adsorption of the  $C_{60}@AgCl-LDO$  nanoparticles was 18% after 1 h. The degradation rate of BPA is 90% by using  $C_{60}@AgCl-LDO$  after 5 h, which is 50% for  $C_{60}@AgCl$ . The degradation efficiency of BPA by using  $C_{60}@AgCl-LDO$  is best in a comparison with other materials. The visible light irradiation becomes a key

factor in exciting the photocatalytic activity of  $C_{60}@AgCl-LDO$  and promoting the fast photocatalytic degradation of BPA. This is due to the visible light absorbing capability, and high photocatalytic efficiency of LDO/ $C_{60}$ -5% will be further accelerated by Ag [20,21,39].

It is well known that the Langmuir-Hinshelwood model (L-H model) is commonly used to describe the kinetics of photocatalytic degradation of organic pollutants in aqueous dispersion [13]. The L-H model can be expressed as follows:

$$r = -\frac{dC}{dt} = kr \frac{K_a C}{1 + K_a C} \quad (1)$$

where  $r$  is the degradation rate of BPA,  $C$  is the BPA concentration in the solution,  $t$  is the reaction time,  $kr$  is the intrinsic rate constant, and  $K_a$  is the adsorption equilibrium constant. When the initial concentration of organic pollutants was low and the adsorption was relatively weak, the factor  $K_a C$  was negligible. In this situation, Eq. (1) can be simplified to the first-order kinetic reaction.

$$r = -\frac{dC}{dt} = k_{app} C \quad (2)$$

When  $t = 0$ ,  $C = C_0$ , and  $C_0$  were the initial concentrations of BPA after achieving adsorption-desorption equilibrium, integration of Eq. (2) can lead out the following equation:

$$\ln \frac{C_0}{C} = k_{app} t \quad (3)$$

where  $k_{app}$  is the apparent pseudo-first-order rate constant, as the basic kinetic parameter for different photocatalysts. When the plot of  $\ln(C_0/C)$  versus irradiation time results in a straight line, its slope would be equal to  $k_{app}$ . According to Fig. 11b, it was clear that the catalyst of  $C_{60}@AgCl-LDO$  exhibited the highest photo-degradation efficiency. Due to the characteristics of  $C_{60}$  and Ag, the  $C_{60}@AgCl-LDO$  will benefit the fast electron transfer and charge separation.

#### 3.2.2. Effect of solution pH

The average results of BPA degradation by using  $C_{60}@AgCl-LDO$  nanoparticles in various initial pH solutions from three repeated batches were plotted in Fig. 12. The effect of pH on the photocatalytic degradation was studied in the pH range from 3.2 to 11.0. When the pH was 5.0, the conversion of BPA was 95%, it was statistically significant with  $C_{60}@AgCl-LDO$  nanoparticles in the neutral  $H_2O$ . About 50% BPA



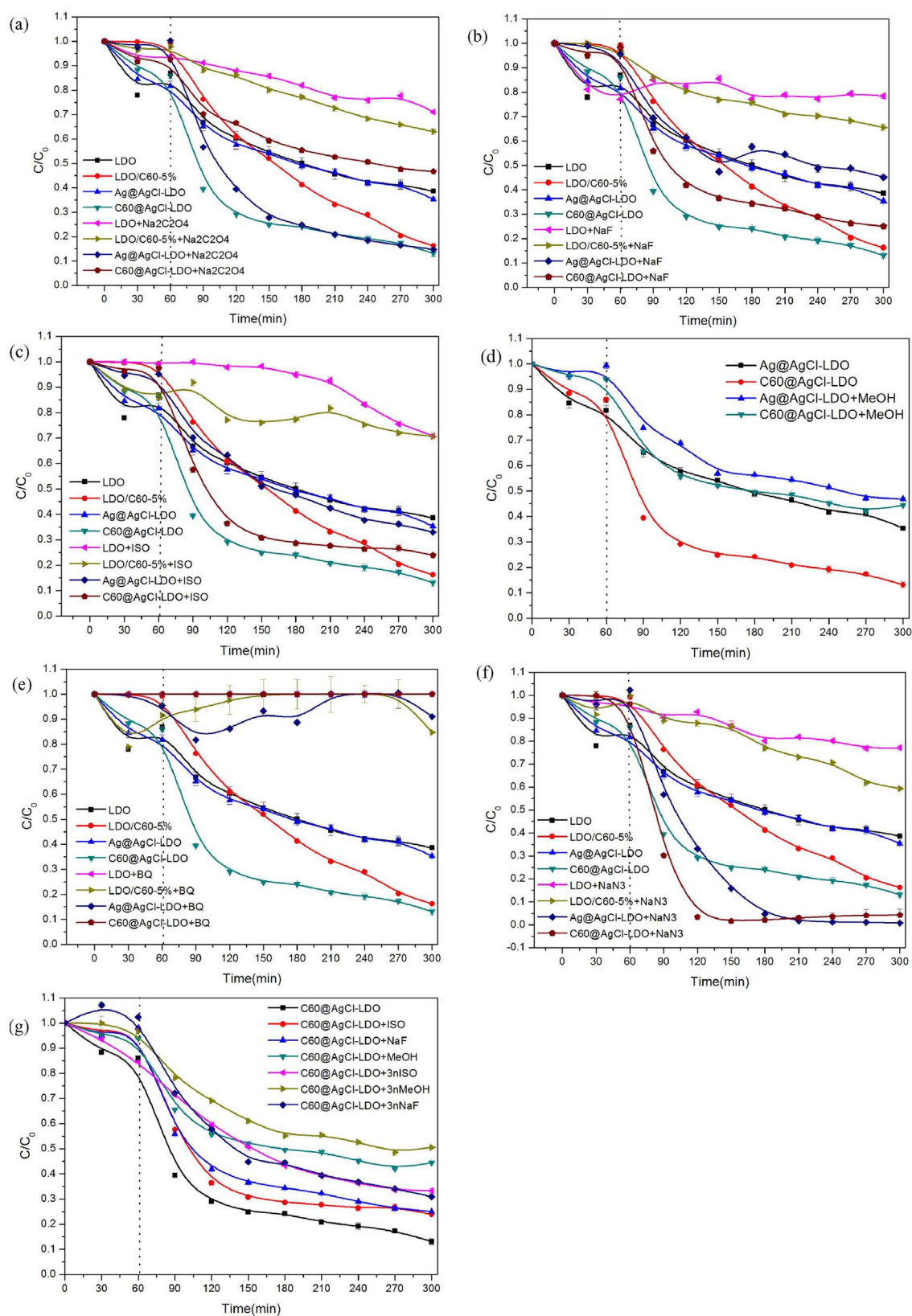


**Fig. 13.** Photocatalytic degradation of BPA by the LDO, LDO/C60-5%, Ag@AgCl-LDO and C60@AgCl-LDO under simulated solar irradiation in the presence of different radical scavenging species. (a) Sodium oxalate ( $\text{Na}_2\text{C}_2\text{O}_4$ ); (b) sodium fluoride (NaF); (c) isopropanol; (d) methanol (MeOH) (e) benzoquinone (BQ) and (f) sodium azide ( $\text{NaN}_3$ ); (g) the effect of different concentrations about radical scavenger in C60@AgCl-LDO.

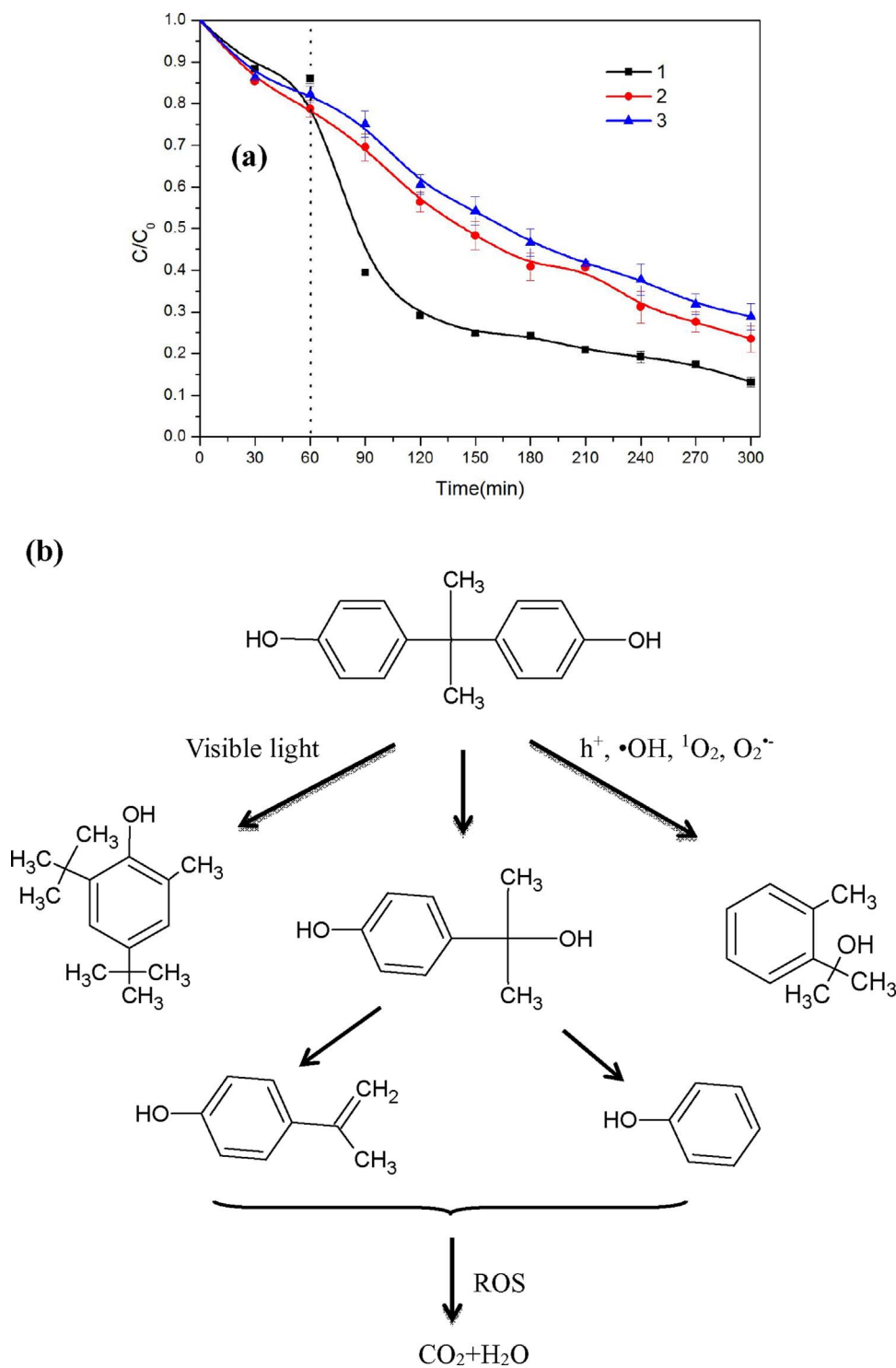


**Fig. 14.** (a) Degradation of BPA in consecutive runs using the recycled  $C_{60}@AgCl$ -LDO (experimental conditions: 10 mg/L BPA, reaction dose 0.5 g/L, temperature 28 °C). Each data represents mean  $\pm$  standard error ( $n = 3$ ). (b) The possible reaction pathway for BPA degradation (ROS: reactive oxygen species).

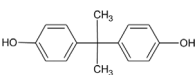
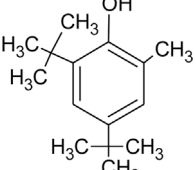
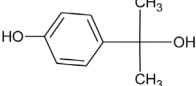
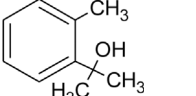
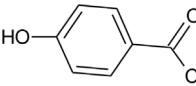
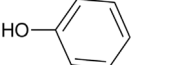
was degraded at the initial pH of 11.0 during 300 min reaction, and about 60% was degraded at the initial pH of 3.2, and about 90% was degraded at the initial pH of 7.0. According to the literatures, it has already been reviewed that acid-base property of the metal oxide surfaces can have considerable effect upon their photocatalytic activity [13]. The acidic medium is beneficial to the formation of  $\cdot OH$  radical in the reaction between dissolved oxygen and excited state electron, which makes the degradation effect of BPA remarkable. But many  $H^+$  added into the solutions would reduce the content of electron. On the other hand, in high pH values, a decreasing of the photo-degradation efficiency is observed and this could possibly be due to the fact that the

increasing of the pH causes a cathodic displacement of the valence band position of the metal oxide in the photocatalyst, which leads to weaken the oxidation ability of the holes [26,27].

### 3.2.3. Effect of radical scavenger about photocatalytic reaction mechanism

A series of batch experiments were performed to examine the photocatalytic reaction mechanisms by using different materials. They were responsible for the degradation of BPA under simulated visible light irradiation by adding different scavengers. Sodium oxalate ( $Na_2C_2O_4$ ) as scavenger was for hole [41], and NaF was for  $\cdot OH_{ads}$  [42]. ISO and methanol as scavengers were for  $\cdot OH_{bulk}$ , which was the  $\cdot OH$

**Table 3**  
BPA and its oxidation intermediates determined by GC–MS analysis.

number	name	Molecular structure	Molecular weight	Mass fragmentation values( <i>m/z</i> )
1	4,4'-(1-methylethylidene)bisPhenol		228	27, 39, 51, 65, 77, 91, 99, 119, 135, 152, 165, 195, 213, 228
2	4,6-di(1,1-dimethylethyl)-2-methyl- Phenol		220	15, 27, 41, 55, 57, 81, 91, 105, 121, 149, 161, 177, 189, 205, 220
3	4-hydroxyphenyl-2-propanol		152	65, 91, 107, 135, 152, 165, 213
4	2-(2-Methylphenyl)-2-propanol		150	41, 43, 59, 77, 91, 105, 118, 133, 150
5	4-isopropenylphenol		134	14, 27, 41, 51, 65, 77, 94, 105, 119, 134
6	Phenol		94	13, 27, 39, 55, 66, 74, 94

in the aqueous suspension [43,44]. Benzoquinone (BQ) was for superoxide radical species [45,46], and  $\text{NaN}_3$  as scavenger for singlet oxygen [47,48] in the reaction system.

10 mM  $\text{Na}_2\text{C}_2\text{O}_4$  were applied to evaluate the contribution of hole in photocatalytic degradation of BPA by different materials, as shown in Fig. 13a. The  $\text{C}_{60}/\text{AgCl}$  decreased electron-hole recombination, the holes might contribute to the photocatalytic degradation of BPA in a certain extent [23,24]. As the hole was generated on the surface of photocatalyst, the photocatalytic degradation of BPA might occur on the surface of photocatalyst by using photocatalytic materials. The photocatalytic degradation of BPA was significantly decreased by adding 10 mM NaF in the solution at different materials, as shown in Fig. 13b. This suggested that  $\cdot\text{OH}_{\text{ads}}$  plays an important role in the photocatalytic degradation of BPA.

Isopropanol and methanol are usually employed as a diagnostic tool of  $\cdot\text{OH}_{\text{bulk}}$  mediated mechanism because it can be easily oxidized by  $\cdot\text{OH}$  and has poor affinity to semiconductor surface in aqueous media [49]. 5% Isopropanol and methanol were respectively dosed to assess their effects on the photodegradation of BPA in different materials. According to Fig. 13c, isopropanol showed a certain inhibitory effects on the photocatalytic efficiency. These results indicated that the  $\cdot\text{OH}_{\text{bulk}}$  had a certain influence in the photocatalytic process, but it had no influence on  $\text{Ag}@\text{AgCl-LDO}$ . Thus, the photogenerated holes on the surface of the  $\text{C}_{60}$  can be directly oxidizing adsorbed  $\cdot\text{OH}$  groups to  $\cdot\text{OH}$ , while the Ag can not. Fig. 13d showed that the  $\text{Ag}@\text{AgCl}$  had a little effect of  $\cdot\text{OH}_{\text{bulk}}$  on the photocatalytic efficiency, but the  $\text{C}_{60}$  on the LDO had more influence on the photocatalytic process about  $\cdot\text{OH}_{\text{bulk}}$ . So the  $\cdot\text{OH}_{\text{bulk}}$  played an important role in the photocatalytic degradation of BPA by using  $\text{C}_{60}/\text{AgCl-LDO}$ .

When 0.5 mM BQ was added in the reaction system, the removal efficiency of BPA significantly decreased (Fig. 13e). Moreover, the inhibitory effect was more obvious with the addition of BQ compared to other scavengers. This result reflected that superoxide radicals might be an indispensable active species responsible for the photocatalytic reaction. Ag and  $\text{ZnAlTi-LDO}$ , as a trap of the photogenerated electrons, could efficiently pass electrons to  $\text{O}_2$  in the solution to produce superoxide radicals ( $\text{O}_2^{\cdot-}$ ), which may react with  $\text{H}^+$  to form  $\text{HO}\cdot_2$ . It was

reported that superoxide radicals, such as  $\text{O}_2^{\cdot-}$  and  $\text{HO}\cdot_2$ , were very active radicals for the ring cleavage of aromatic compounds [48,49]. The singlet oxygen ( $^1\text{O}_2$ ) is known as one of the highly reactive oxygen species via the energy or transfer electron [45]. The formation of  $^1\text{O}_2$  can be detected by direct method such as nearinfrared phosphorescence, or indirect method based on use of probe reagent.  $\text{NaN}_3$  is an effective scavenger of  $^1\text{O}_2$  and in this study 10 mM  $\text{NaN}_3$  was added in the reaction system as shown in Fig. 13f [48,50–53]. The photocatalytic degradation of BPA decreased by using the  $\text{LDO}/\text{C}_{60}$ -5%, but it increased by the materials with Ag-added. It implied that the  $\text{N}_3^-$  combined with  $\text{Ag}^+$  the  $\text{N}_3^-$  can influence the photocatalytic degradation of BPA. These results indicated that the contribution of  $^1\text{O}_2$  towards BPA degradation can not be ignored in the photocatalytic process under simulated visible light irradiation.

It can be observe the reaction further with the different concentrations of the scavengers as shown in Fig. 13g. Different concentrations of NaF, isopropanol and methanol were dosed to assess their effects on the photo-degradation of BPA. With the concentrations of scavengers increased, the photocatalytic efficiency of BPA decreased. In conclusion, the  $\text{C}_{60}$  and Ag transferred the  $\text{O}_2$  to produce superoxide radicals ( $\text{O}_2^{\cdot-}$ ) in the photogenerated electrons. The photogenerated holes, superoxide radicals,  $\cdot\text{OH}_{\text{bulk}}$ , singlet oxygen and  $\cdot\text{OH}_{\text{ads}}$  could degrade BPA efficiently.

### 3.3. Cycling photodegradation, mineralization and photocatalytic degradation pathway of BPA

As shown in Fig. 14a, the BPA can be degraded up to 90% by  $\text{C}_{60}/\text{AgCl-LDO}$  under simulated visible light irradiation within 5 h. Additionally, the  $\text{C}_{60}/\text{AgCl-LDO}$  can be easily separated for recycling, and the catalyst maintains good photoactivity after 3 cycles. The TOC analysis of the irradiated solution was performed in order to get complementary information of the degree of mineralization achieved by the photocatalysts. The results suggest that the composite displays high efficiency to degrade BPA and to mineralize BPA to organic acids,  $\text{CO}_2$  and  $\text{H}_2\text{O}$ . The probable intermediates formed in the degradation process were identified by GC–MS. GC chromatograms of the prepared



samples indicated the presence of different species in the samples, and we have identified six of them according to mass fragmentation values and comparing the mass spectrums with that of the known substances (Table 3). The intermediates formed in the degradation of BPA process were 4-hydroxyphenyl-2-propanol, 4,6-di(1,1-dimethylethyl)-2-methyl-Phenol, 4-isopropenylphenol, 2-(2-Methylphenyl)-2-propanol and Phenol. The 4-isopropenylphenol and 2-(2-Methylphenyl)-2-propanol could be attributable to the attack of BPA by photogenerated holes at the *tert*-butyl carbon. In addition, superoxide radical species and singlet oxygen could also directly oxidize BPA and intermediates [54]. Fig. 14b illustrates the simple degradation pathway of BPA by C<sub>60</sub>@AgCl-LDO.

#### 4. Conclusions

In summary, the C<sub>60</sub>@AgCl-LDO was successfully prepared by the coprecipitation-light-induced method. As for C<sub>60</sub>@AgCl-LDO sample, the recombination of photoinduced electron-hole pairs was inhibited greatly due to the superior electrical conductivity of C<sub>60</sub> and the strong coupling between ZnAl<sub>2</sub>O<sub>4</sub> and C<sub>60</sub>@AgCl. Due to the characteristics of C<sub>60</sub> and Ag, the C<sub>60</sub>@AgCl-LDO will benefit the fast electron transfer and charge separation. As for Ag-added photocatalysts, the decreased electron-hole recombination is contributed mainly by the changed surface states of materials. The degradation rate of the as-synthesized C<sub>60</sub>@AgCl-LDO in photocatalytic degradation of BPA under simulated visible light irradiation was 90%, and the photocatalysts with remarkable photocatalytic activity can be used for large-scale environmental remediation. According to the experiments, photo-generated holes, superoxide radical species, singlet oxygen and  $\cdot\text{OH}_{\text{bulk}}$  were responsible for the photo-degradation, among which the superoxide radical species played an indispensable role in the photocatalytic reaction system. Moreover, the removal rate of BPA achieved 100% by using C<sub>60</sub>@AgCl-LDO under ultraviolet light in 5 min, which proved that the materials of C<sub>60</sub>@AgCl-LDO can be used as major environmental remediations.

#### Acknowledgements

Funding: The authors are thankful to the financial support by the National Science Foundation of China (Grant Nos. 41673092, 41472038, 41273122), the Science and Technology Plan of Guangdong Province, China (Nos. 2014A020216002, 2016B020242004), Guangdong special support program for millions of leading engineering talents (No. 201626011) and Science and Technology Program of Guangzhou, China (No. 201604020064).

#### References

- G.D. Bittner, C.Z. Yang, M.A. Stoner, Estrogenic chemicals often leach from BPA-free plastic products that are replacements for BPA-containing poly-carbonate products, *Environ. Health* 3 (2014) 1–14.
- H. Kuang, H. Yin, L. Liu, L. Xu, W. Ma, C. Xu, Asymmetric plasmonic aptasensor for sensitive detection of bisphenol A, *ACS Appl. Mater. Interfaces* 6 (1) (2014) 364–369.
- E. Chung, J. Jeon, J. Yu, C. Lee, Surface-enhanced Raman scattering aptasensor for ultrasensitive trace analysis of bisphenol A, *Biosens. J. Choo Biosens. Bioelectron.* 64 (2015) 560–565.
- A. Schecter, N. Malk, D. Haffner, S. Smith, T. Harris, O. Paepke, L. Birnbaum, Bisphenol A (BPA) in U.S. Food, *Environ. Sci. Technol.* 44 (2010) 9425–9430.
- E. Diamanti-Kandarakis, J.P. Bourguignon, L.C. Giudice, R. Hauser, G.S. Prins, A.M. Soto, Endocrine-disrupting chemicals: an endocrine society scientific statement, *Endocr. Rev.* 30 (4) (2009) 293–342.
- A.C. Gore, V.A. Chappell, S.E. Fenton, J.A. Flaws, A. Nadal, G.S. Prins, Executive summary to EDC-2: the endocrine society's second scientific statement on endocrine-disrupting chemicals, *Endocr. Rev.* 36 (6) (2015) 593–602.
- A.M. Calafat, X. Ye, L.Y. Wong, J.A. Reidy, L.L. Needham, Exposure of the U.S. population to bisphenol A and 4-tertiary-octylphenol: 2003–2004, *Environ. Health Perspect.* 116 (1) (2008) 39–44.
- F.S. Vom Saal, C. Hughes, An extensive new literature concerning low-dose effects of bisphenol A shows the need for a new risk assessment, *Environ. Health Perspect.* 113 (8) (2005) 926–933.
- B. Pan, D.H. Lin, H. Mashayekhi, B.S. Xing, Adsorption and hysteresis of bisphenol

- A and 17 alpha-ethinyl estradiol on carbon nanomaterials, *Environ. Sci. Technol.* 42 (2008) 5480–5485.
- Y.H. Cui, X.Y. Li, G.H. Chen, Electrochemical degradation of bisphenol A on different anodes, *Water Res.* 43 (2009) 1968–1976.
- E.M. Rodriguez, G. Fernandez, N. Klammer, M.I. Maldonado, P.M. Alvarez, S. Malato, Efficiency of different solar advanced oxidation processes on the oxidation of bisphenol A in water, *Appl. Catal. B* 95 (2010) 228–237.
- Y.T. Xie, H.B. Li, L. Wang, Q.A. Liu, Y. Shi, H.Y. Zheng, M. Zhang, Y.T. Wu, B. Lu, Molecularly imprinted polymer microspheres enhanced biodegradation of bisphenol A by acclimated activated sludge, *Water Res.* 45 (2011) 1189–1198.
- X.R. Wang, P.X. Wu, Z.J. Huang, N.W. Zhu, J.H. Wu, P. Li, Z. Dang, Solar photocatalytic degradation of methylene blue by mixed metal oxide catalysts derived from ZnAl<sub>2</sub>O<sub>4</sub> layered double hydroxides, *Appl. Clay Sci.* 95 (2014) 95–103.
- J. Li, C. Yu, C. Zheng, A. Etogo, Y. Xie, Y. Zhong, Y. Hu, Facile formation of Ag<sub>2</sub>WO<sub>4</sub>/AgX (X = Cl, Br, I) hybrid nanorods with enhanced visible-light-driven photoelectrochemical properties, *Mater. Res. Bull.* 61 (2015) 315.
- J. Li, Y. Xie, Y. Zhong, Y. Hu, Facile synthesis of Z-scheme Ag<sub>2</sub>CO<sub>3</sub>/Ag/AgBr ternary heterostructured nanorods with improved photostability and photoactivity, *J. Mater. Chem. A* 3 (2015) 5474.
- C. Shen, Q. Zhu, Z. Zhao, T. Wen, X. Wang, A. Xu, Plasmon enhanced visible light photocatalytic activity of ternary Ag<sub>2</sub>MoO<sub>7</sub>@AgBr-Ag rod-like heterostructure, *J. Mater. Chem. A* 3 (2015) 14661.
- C. Zeng, Y.M. Hu, Y.X. Guo, T.R. Zhang, F. Dong, Y.H. Zhang, H.W. Huang, Facile in situ self-sacrifice approach to ternary hierarchical architecture Ag/AgX (X = Cl, Br, I)/Ag<sub>2</sub>O<sub>3</sub> distinctively promoting visible-light photocatalysis with composition-dependent mechanism, *ACS Sustain. Chem. Eng.* 4 (2016) 3305.
- H. Jiang, J.K. Liu, J.D. Wang, Y. Lu, X.H. Yang, Thermal perturbation nucleation and growth of silver molybdate nanoclusters by a dynamic template route, *Cryst. Eng. Comm.* 17 (2015) 5511.
- L. Liu, S. Lin, J. Hu, Y. Liang, W. Cui, Plasmon-enhanced photocatalytic properties of nano Ag@AgBr on single-crystalline octahedral Cu<sub>2</sub>O {111} microcrystals heterostructure photocatalyst, *Appl. Surf. Sci.* 330 (2015) 94.
- F. Dong, Z. Zhao, Y. Sun, S. Zhang, S. Yan, Z. Wu, An advanced semimetal-organic Bi Spheres-g-C<sub>3</sub>N<sub>4</sub> nanohybrid with SPR-enhanced visible-light photocatalytic performance for NO purification, *Environ. Sci. Technol.* 49 (2015) 12432.
- X. Xiao, G. Ge, C. Han, Y. Li, Z. Zhao, Y. Xin, S. Fang, L. Wu, P.A. Qiu, facile way to synthesize Ag@AgBr cubic cages with efficient visible-light-induced photocatalytic activity, *Appl. Catal. B* 163 (2015) 564.
- H. Wang, J. Gao, T. Guo, R. Wang, L. Guo, Y. Liu, J. Li, Facile synthesis of AgBr nanoparticles with exposed {111} facets and enhanced photocatalytic properties, *Chem. Commun.* 48 (2012) 275.
- Q. Dong, Z. Jiao, H. Yu, J. Ye, Y. Bi, Facile synthesis of hollow Ag@AgBr heterostructure with highly efficient visible-light photocatalytic properties, *Cryst. Eng. Comm.* 16 (2014) 8317.
- H. Shi, G. Li, H. Sun, T. An, H. Zhao, P.K. Wong, Visible light-driven photocatalytic inactivation of *E. coli* by Ag/AgX-CNTs (x = Cl, Br, I) plasmonic photocatalysts: bacterial performance and deactivation mechanism, *Appl. Catal. B* 158 (2014) 301.
- M. Abou Asi, L. Zhu, C. He, V.K. Sharma, D. Shu, S. Li, J. Yang, Y. Xiong, Visible-light-harvesting reduction of CO<sub>2</sub> to chemical fuels with plasmonic Ag@AgBr/CNT nanoheterostructure, *Catal. Today* 216 (2013) 268.
- F. Jing, Y. Zhang, S. Luo, W. Chu, W. Qian, Nano-size MZnAl (M = Cu, Co, Ni) metal oxides obtained by combining hydrothermal synthesis with urea homogeneous precipitation procedures, *Appl. Clay Sci.* 48 (2010) 203–207.
- R.K. Sahu, B.S. Mohanta, N.N. Das, Synthesis, characterization and photocatalytic activity of mixed oxides derived from ZnAl<sub>2</sub>O<sub>4</sub> ternary layered double hydroxides, *J. Phys. Chem. Solids* 74 (2013) 1263–1270.
- H. Zhang, F.Z. Zhang, L.L. Ren, D.G. Evans, X. Duan, Synthesis of layered double hydroxide anionic clays intercalated by carboxylate anions, *Mater. Chem. Phys.* 85 (2004) 207–214.
- S. Luo, S.G. Yang, C. Sun, J.D. Gu, Improved debromination of polybrominated diphenyl ethers by bimetallic iron-silver nanoparticles coupled with microwave energy, *Sci. Total Environ.* 429 (2012) 300–308.
- S.S. Narwade, B.B. Mulik, S.M. Mali, B.R. Sathe, Silver nanoparticles sensitized C<sub>60</sub>(Ag@C<sub>60</sub>) as efficient electrocatalysts for hydrazine oxidation: implication for hydrogen generation reaction, *Appl. Surf. Sci.* 396 (2017) 939–944.
- F.B.D. Saiah, B.L. Su, N. Bettahar, Nickel-iron layered double hydroxide (LDH): textural properties upon hydrothermal treatments and application on dye sorption, *J. Hazard. Mater.* 165 (2009) 206–217.
- W.H. Zhang, X.D. Guo, J. He, Z.Y. Qian, Preparation of Ni(II)/Ti(IV) layered double hydroxide at high supersaturation, *J. Eur. Ceram. Soc.* 28 (2008) 1623–1629.
- F. Zhang, X. Xiang, F. Li, X. Duan, Layered double hydroxides as catalytic materials: recent development, *Catal. Surv. Asia* 12 (2008) 253–265.
- J.S. Valente, F. Tzompantzi, J. Prince, J.G.H. Cortez, R. Gomez, Adsorption and photocatalytic degradation of phenol and 2,4 dichlorophenoxyacetic acid by Mg-Zn-Al layered double hydroxides, *Appl. Catal. B Environ.* 90 (2009) 330–338.
- C. Han, N. Zhang, Y.J. Xu, Structural diversity of graphene materials and their multifarious roles in heterogeneous photocatalysis, *Nano Today* 1 (2016) 351–372.
- S.S. Yang, P.X. Wu, M.Q. Chen, Z.J. Huang, W. Li, N.W. Zhu, Y.R. Jia, Enhanced photo-degradation of bisphenol A under simulated solar light irradiation by Zn-Ti mixed metal oxides loaded on graphene from aqueous media, *RSC Adv.* 6 (2016) 26495–26504.
- G. Reenamole, K.S. Michael, C.P. Suresh, A highly efficient Ag-ZnO photocatalyst: synthesis, properties, and mechanism, *J. Phys. Chem. C* 112 (2008) 13563–13570.
- Y.J. Xu, Y.B. Zhuang, X.Z. Fu, New insight for enhanced photocatalytic activity of TiO<sub>2</sub> by doping carbon nanotubes: a case study on degradation of benzene and methyl orange, *J. Phys. Chem. C* 114 (2010) 2669–2676.

- [39] T.T. Li, S.L. Luo, Y. Luo, L.X. Yang, Ag/AgI nanoparticles decorated WO<sub>3</sub>/TiO<sub>2</sub> nanotubes with enhanced visible light photocatalytic activity, *Mater. Lett.* 180 (2016) 130–134.
- [40] Y.Y. Bai, F.R. Wang, J.K. Liu, A new complementary catalyst and catalytic mechanism: Ag<sub>2</sub>MoO<sub>4</sub>/Ag/AgBr/GO heterostructure, *Ind. Eng. Chem. Res.* 55 (2016) 9873–9879.
- [41] C.L. Tang, H.W. Bai, L. Liu, X.L. Zan, P. Gao, D.D. Sun, W. Yan, A green approach assembled multifunctional Ag/AgBr/TNF membrane for clean water production & disinfection of bacteria through utilizing visible light, *Appl. Catal. B: Environ.* 196 (2016) 57–67.
- [42] S. Song, L. Xu, Z. He, J. Chen, X. Xiao, B. Yan, Mechanism of the photocatalytic degradation of C. I. reactive black 5 at pH 12. 0 using SrTiO<sub>3</sub>/CeO<sub>2</sub> as the catalyst, *Environ. Sci. Technol.* 41 (2007) 5846–5853.
- [43] W. Wang, Y. Yu, T. An, G. Li, H.Y. Yip, J.C. Yu, P.K. Wong, Visible-light-driven photocatalytic inactivation of E. coli K-12 by bismuth vanadate nanotubes: bactericidal performance and mechanism, *Environ. Sci. Technol.* 46 (2012) 4599–4606.
- [44] C. Wang, L. Zhu, M. Wei, P. Chen, G. Shan, Photolytic reaction mechanism and impacts of coexisting substances on photodegradation of bisphenol A by Bi<sub>2</sub>WO<sub>6</sub> in water, *Water Res.* 46 (2012) 845–853.
- [45] Y.Y. Li, J.S. Wang, B. Liu, L.Y. Dang, H.C. Yao, Z.J. Li, BiOI-sensitized TiO<sub>2</sub> in phenol degradation: a novel efficient semiconductor sensitizer, *Chem. Phys. Lett.* 508 (2011) 102–106.
- [46] M. Yin, Z. Li, J. Kou, Z. Zou, Mechanism investigation of visible light-induced degradation in a heterogeneous TiO<sub>2</sub>/Eosin Y/Rhodamine B system, *Environ. Sci. Technol.* 43 (2009) 8361–8366.
- [47] H. Ji, F. Chang, X. Hu, W. Qin, J. Shen, Photocatalytic degradation of 2,4,6-trichlorophenol over g-C<sub>3</sub>N<sub>4</sub> under visible light irradiation, *Chem. Eng. J.* 218 (2013) 183–190.
- [48] J.W. Ng, X.P. Wang, D.D. Sun, One-pot hydrothermal synthesis of a hierarchical nanofungus-like anatase TiO<sub>2</sub> thin film for photocatalytic oxidation of bisphenol A, *Appl. Catal. B* 110 (2011) 260–272.
- [49] L.S. Zhang, K.H. Wong, H.Y. Yip, C. Hu, J.C. Yu, C.Y. Chan, P.K. Wong, Effective photocatalytic disinfection of E.coli K-12 using AgBr-Ag-Bi<sub>2</sub>WO<sub>6</sub> nanojunction system irradiated by visible light: the role of diffusing hydroxyl radicals, *Environ. Sci. Technol.* 44 (2010) 1392–1398.
- [50] Y. Nosaka, T. Daimon, A.Y. Nosaka, Y. Murakami, Singlet oxygen formation in photocatalytic TiO<sub>2</sub> aqueous suspension, *Phys. Chem. Chem. Phys.* 6 (2004) 2917–2918.
- [51] X.P. Wang, T.T. Lim, Effect of hexamethylenetetramine on the visible-light photocatalytic activity of C-N codoped TiO<sub>2</sub> for bisphenol A degradation: evaluation of photocatalytic mechanism and solution toxicity, *Appl. Catal. A* 399 (2011) 233–241.
- [52] P. Raja, A. Bozzi, H. Mansilla, J. Kiwi, Evidence for superoxide-radical anion, singlet oxygen and OH-radical intervention during the degradation of the lignin model compound (3-methoxy-4-hydroxyphenylmethylcarbinol), *J. Photochem. Photobiol. A* 169 (2005) 271–278.
- [53] D. Zhang, R. Qiu, L. Song, B. Eric, Y. Mo, X. Huang, Role of oxygen active species in the photocatalytic degradation of phenol using polymer sensitized TiO<sub>2</sub> under visible light irradiation, *J. Hazard. Mater.* 163 (2009) 843–847.
- [54] C. Chang, L.Y. Zhu, Y. Fu, X.L. Chu, Highly active Bi/BiOI composite synthesized by one-step reaction and its capacity to degrade bisphenol A under simulated solar light irradiation, *Chem. Eng. J.* 233 (2013) 305–314.
- [55] E. Fileti, G. Colherinhas, T. Malaspina, Predicting the properties of a new class of Host-guest complexes: C<sub>60</sub> fullerene and CB[9] cucurbituril, *Phys. Chem. Chem. Phys.* 16 (2014) 22823–22829.